nature physics

SUPPLEMENTARY INFORMATION
https://doi.org/10.1038/s41567-019-0535-3

In the format provided by the authors and unedited.

Avoided quasiparticle decay from strong quantum interactions

Ruben Verresen[1,2,3]*, Roderich Moessner[1] and Frank Pollmann[2,4]

[1]Max-Planck-Institute for the Physics of Complex Systems, Dresden, Germany. [2]Department of Physics, Technische Universität München, Garching, Germany. [3]Kavli Institute for Theoretical Physics, University of California, Santa Barbara, CA, USA. [4]Munich Center for Quantum Science and Technology (MCQST), Munich, Germany. *e-mail: rubenverresen@gmail.com

Supplemental Materials: "Avoided quasiparticle decay from strong quantum interactions"

I. THE INTERACTING SINGLE-PARTICLE GREEN'S FUNCTION AND SPECTRAL FUNCTION

We will first calculate $G(E) = \langle\psi|(E-\hat{H})^{-1}|\psi\rangle$. If we think of $E-\hat{H}$ as a matrix (with indices labeled by $|\psi\rangle$ and $|\varphi_\alpha\rangle$), then $G(E)$ is the top left element of its inverse. This is easily calculated. Schematically, first write

$$E-\hat{H} = \begin{pmatrix} A & B \\ C & D \end{pmatrix} \text{ with } A = E - E_b, \quad D_{\alpha\beta} = (E-E_\alpha)\,\delta(\alpha-\beta) \quad \text{and } B_\alpha = C_\alpha = -\gamma. \tag{S1}$$

Since D is diagonal, one can apply the well-known result that

$$\det(E-\hat{H}) = \det(A - BD^{-1}C)\det D = \left(E - E_b - \gamma^2 \int \mathrm{d}\alpha \frac{1}{E-E_\alpha}\right)\det D. \tag{S2}$$

Finally, by Cramer's rule, we can express

$$G(E) = \langle\psi|(E-\hat{H})^{-1}|\psi\rangle = \frac{\det D}{\det(E-\hat{H})} = \frac{1}{E - E_b - \gamma^2 g(E)}, \tag{S3}$$

where we have introduced the Cauchy principal value $g(E) := \int_0^\infty \frac{\nu(\varepsilon)}{E-\varepsilon}\mathrm{d}\varepsilon$, as in the main text.

Note that

$$g(E - i\eta) = \int_0^\infty \nu(\varepsilon)\frac{E-\varepsilon+i\eta}{(E-\varepsilon)^2+\eta^2}\mathrm{d}\varepsilon, \text{ hence } \frac{1}{\pi}\mathrm{Im}\, g(E-i0^+) = \int_0^\infty \nu(\varepsilon)\,\delta(E-\varepsilon) = \nu(E). \tag{S4}$$

In other words, $g(E-i0^+) = g(E) + i\pi\nu(E)$.

We can now calculate $\mathcal{A}(E) = \frac{1}{\pi}\mathrm{Im}G(E-i0^+)$ as follows,

$$\mathcal{A}(E) = \frac{1}{\pi}\mathrm{Im}\left(\frac{1}{E - E_b - \gamma^2 g(E-i0^+) - i0^+}\right) \tag{S5}$$

$$= \frac{1}{\pi}\mathrm{Im}\left(\frac{1}{E - E_b - \gamma^2 g(E) - i\pi\gamma^2\nu(E) - i0^+}\right) \tag{S6}$$

$$= \begin{cases} \frac{\gamma^2\nu(E)}{(E-E_b-\gamma^2 g(E))^2 + (\pi\gamma^2\nu(E))^2} & \text{if } \nu(E) \neq 0, \\ \delta(E - E_b - \gamma^2 g(E)) & \text{if } \nu(E) = 0. \end{cases} \tag{S7}$$

II. TWO-PARTICLE DOS

A. Quadratic dispersion

Here we calculate the two-particle DOS in various dimensions D for the single-particle dispersion

$$\varepsilon_{\boldsymbol{k}} = \Delta + \frac{|\boldsymbol{k}|^2}{2m}. \tag{S8}$$

1. $D=1$

$$\rho_2^{(1D)}(k,\varepsilon) \propto \int \delta(\varepsilon_q + \varepsilon_{k-q} - \varepsilon)\,\mathrm{d}q = \int \delta\left(2\Delta - \varepsilon + \frac{q^2}{2m} + \frac{(k-q)^2}{2m}\right)\,\mathrm{d}q \tag{S9}$$

$$= \int \delta\left(2\Delta - \varepsilon + \frac{1}{2m}\left[2\left(q - \frac{k}{2}\right)^2 + \frac{k^2}{2}\right]\right)\,\mathrm{d}q \tag{S10}$$

$$\propto \left.\frac{1}{\frac{1}{m}\times\left|q-\frac{k}{2}\right|}\right|_{|q-k/2|=\sqrt{m(\varepsilon-2\Delta)-k^2/4}} = \frac{\sqrt{m}}{\sqrt{\varepsilon - 2\Delta - k^2/4m}}. \tag{S11}$$

2. $D = 2$

$$\rho_2^{(2D)}(\boldsymbol{k},\varepsilon) \propto \int \delta(\varepsilon_{\boldsymbol{q}} + \varepsilon_{\boldsymbol{k}-\boldsymbol{q}} - \varepsilon)\, \mathrm{d}^2\boldsymbol{q} = \int \delta\left(2\Delta - \varepsilon + \frac{q_x^2}{2m} + \frac{q_y^2}{2m} + \frac{(k_x-q_x)^2}{2m} + \frac{(k_y-q_y)^2}{2m}\right) \mathrm{d}q_x \mathrm{d}q_y \tag{S12}$$

$$= \int \rho_2^{(1D)}\left(k_x,\ \varepsilon - \frac{q_y^2}{2m} - \frac{(k_y-q_y)^2}{2m}\right) \mathrm{d}q_y = \int \frac{\sqrt{m}}{\sqrt{\varepsilon - 2\Delta - q_y^2/2m - (k_y-q_y)^2/2m - k_x^2/4m}}\, \mathrm{d}q_y \tag{S13}$$

$$= \int \frac{m}{\sqrt{\left(\varepsilon - 2\Delta - (k_x^2+k_y^2)/4m\right) - (q_y - k_y/2)^2}}\, \mathrm{d}q_y \propto \begin{cases} m & \text{if } \varepsilon > 2\Delta + \frac{k_x^2+k_y^2}{4m}, \\ 0 & \text{otherwise.} \end{cases} \tag{S14}$$

3. $D \geq 3$

$$\rho_2^{(3D)}(\boldsymbol{k},\varepsilon) \propto \int \delta(\varepsilon_{\boldsymbol{q}} + \varepsilon_{\boldsymbol{k}-\boldsymbol{q}} - \varepsilon)\, \mathrm{d}^D\boldsymbol{q} \propto \int \left(\frac{1}{|\partial_\theta \varepsilon_{\boldsymbol{k}-\boldsymbol{q}}|}\ \sin\theta\right)\Bigg|_{\varepsilon_{\boldsymbol{q}}+\varepsilon_{\boldsymbol{k}-\boldsymbol{q}}=\varepsilon} q^{D-1}\mathrm{d}q \tag{S15}$$

Since $|\boldsymbol{k}-\boldsymbol{q}|^2 = k^2 + q^2 - 2kq\cos\theta$, we have that $\partial_\theta \varepsilon_{\boldsymbol{k}-\boldsymbol{q}} = \frac{kq}{m}\sin\theta$. Hence $\rho_2(\boldsymbol{k},\varepsilon) \propto \frac{m}{k}\int q^{D-2}\,\mathrm{d}q$. To determine the range of integration, it is useful to first define δ through $\varepsilon = 2\Delta + \frac{k^2}{4m} + \frac{\delta}{m}$. From the condition that $\varepsilon = \varepsilon_{\boldsymbol{q}} + \varepsilon_{\boldsymbol{k}-\boldsymbol{q}}$ and that $|\cos\theta| \leq 1$, we obtain the condition on q, i.e. $|\sqrt{\delta} - k/2| \leq q \leq \sqrt{\delta} + k/2$. Note that this only makes sense if $\delta \geq 0$, i.e. it is the correct variable to use to describe the onset of the DOS. Plugging this in and using that δ is small, we obtain

$$\rho_2(\boldsymbol{k},\varepsilon) \propto \frac{m}{k}\ q^{D-1}\Big|_{|\sqrt{\delta}-k/2|}^{\sqrt{\delta}+k/2} \propto \frac{m}{k}\, k^{D-1}\ \left[\left(1+\frac{\sqrt{\delta}}{k}\right)^{D-1} - \left(1-\frac{\sqrt{\delta}}{k}\right)^{D-1}\right] \tag{S16}$$

$$\approx \frac{m}{k}\, k^{D-1}\ \left[\left(1+(D-1)\frac{\sqrt{\delta}}{k}\right) - \left(1-(D-1)\frac{\sqrt{\delta}}{k}\right)\right] \approx mk^{D-3}\sqrt{\delta} = m^{3/2}k^{D-3}\sqrt{\varepsilon - 2\Delta - \frac{k^2}{4m}}. \tag{S17}$$

Hence, for $D \geq 3$, the onset always has a square-root onset. *However*, the above derivation is only for a narrow window near the onset, and this window vanishes as one approaches $\boldsymbol{k} \to 0$. Indeed, one can straightforwardly calculate that

$$\rho_2(\boldsymbol{k}=0,\varepsilon) \propto \int \delta\left(2\Delta - \varepsilon + \frac{q^2}{m}\right) q^{D-1}\mathrm{d}q \propto mq^{D-2}\big|_{q^2=m(\varepsilon-2\Delta)} = m^{D/2}\,(\varepsilon - 2\Delta)^{D/2-1}. \tag{S18}$$

This is physically the behaviour that will dominate near $\boldsymbol{k} \approx 0$.

B. Roton minima

We now consider the dispersion relevant to the roton minimum appearing in, for example, superfluid helium,

$$\varepsilon_{\boldsymbol{k}} = \Delta + \frac{1}{2m}(|\boldsymbol{k}| - K)^2. \tag{S19}$$

Here we restrict ourselves to $D \geq 3$, where we can use Eq. (S15). Since $|\boldsymbol{k}-\boldsymbol{q}| = \sqrt{k^2+q^2-2kq\cos\theta}$, we have that

$$\partial_\theta \varepsilon_{\boldsymbol{k}-\boldsymbol{q}} = {}^1\!/\!{}_m \times (|\boldsymbol{k}-\boldsymbol{q}| - K) \times \frac{1}{2|\boldsymbol{k}-\boldsymbol{q}|} \times 2kq\sin\theta. \tag{S20}$$

We are interested in $0 < k < 2K$, where the threshold is near $\varepsilon \approx 2\Delta$, which forces the decay products to be very close to the roton minimum, i.e $q \approx K$ and $|\boldsymbol{k}-\boldsymbol{q}| \approx K$. Hence, near the threshold we have

$$\rho_2(\boldsymbol{k},\varepsilon) \propto m \int \left(\frac{|\boldsymbol{k}-\boldsymbol{q}|}{||\boldsymbol{k}-\boldsymbol{q}|-K|} \right)\Bigg|_{\varepsilon_{\boldsymbol{q}}+\varepsilon_{\boldsymbol{k}-\boldsymbol{q}}=\varepsilon} \frac{q^{D-2}}{k}\,\mathrm{d}q \approx \frac{mK^{D-1}}{k} \int \left(\frac{1}{\sqrt{2m\left(\varepsilon_{\boldsymbol{k}-\boldsymbol{q}}-\Delta\right)}} \right)\Bigg|_{\varepsilon_{\boldsymbol{q}}+\varepsilon_{\boldsymbol{k}-\boldsymbol{q}}=\varepsilon} \mathrm{d}q \tag{S21}$$

$$= \frac{mK^{D-1}}{k} \int_{K-\sqrt{2m(\varepsilon-2\Delta)}}^{K+\sqrt{2m(\varepsilon-2\Delta)}} \frac{1}{\sqrt{2m(\varepsilon-2\Delta)-(q-K)^2}}\mathrm{d}q \tag{S22}$$

$$= \frac{mK^{D-1}}{k} \int_{-1}^{1} \frac{1}{\sqrt{1-x^2}}\mathrm{d}x \quad \left(\text{where } x := \frac{q-K}{\sqrt{2m(\varepsilon-2\Delta)}} \right) \tag{S23}$$

$$\propto \begin{cases} 0 & \text{if } \delta < 0 \\ \frac{mK^{D-1}}{k} & \text{if } \delta > 0 \end{cases} \qquad \text{where } \varepsilon \approx 2\Delta + \delta. \tag{S24}$$

We repeat that the above derivation is for $0 < k < 2K$. We conclude that in this regime, there is a jump discontinuity at the onset.

III. CONVERGENCE OF DMRG

A. Convergence in bond dimension

Fig. S1 shows the spectral function obtained with DMRG for a cylinder with circumference $L_{\mathrm{circ}} = 6$ where we have set the anisotropy parameter $\delta = 0.1$ (to wit, $\delta = 0$ is the isotropic TLHAF). We observe that whilst the lowest-energy mode (near the zone center, Γ) is still converging, the mid- and high-energy regions of the single-magnon branch display convergence.

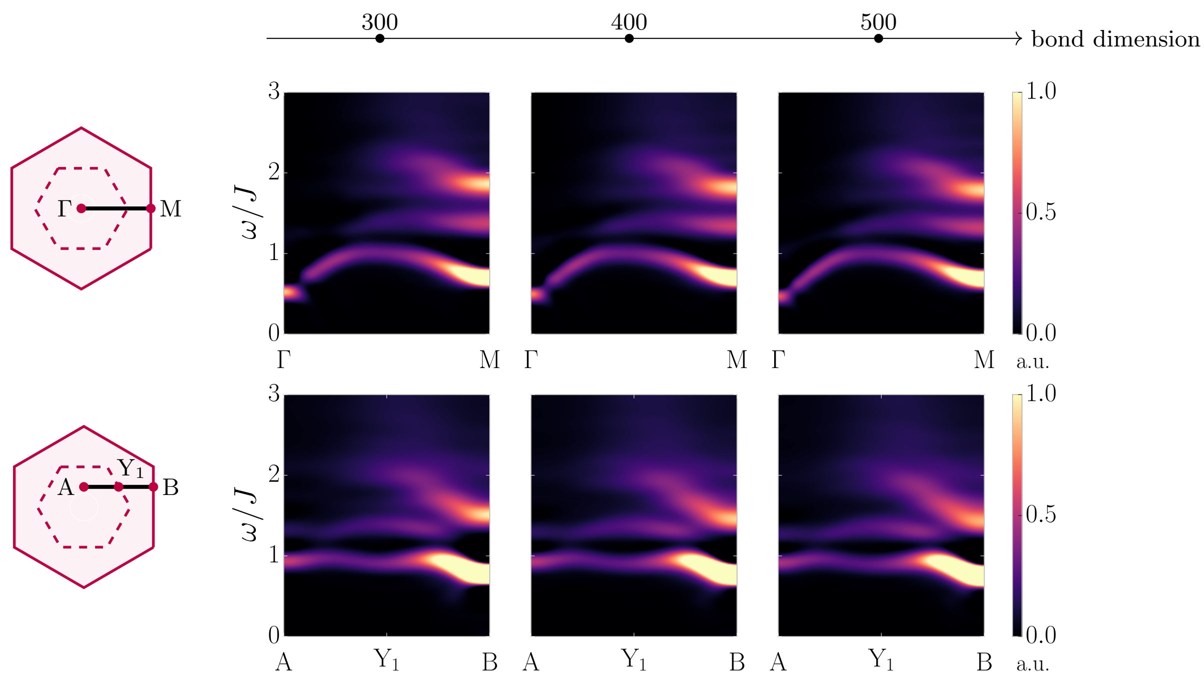

FIG. S1. Comparing the out-of-plane spectral functions for the TLHAF with anisotropy parameter $\delta = 0.1$ for three different bond dimensions.

Fig. S2 shows the analogous data for the anisotropy parameter $\delta = 0.05$—the case studied in the main text. We similarly observe convergence for the mid- and high-energy magnon dispersion.

As discussed in the main text, to conclude that magnon decay is absent, we mainly require the dispersion at such higher energies, supplemented with the value of the gap at the quasi-Goldstone mode at the zone corner, i.e. ε_K. To

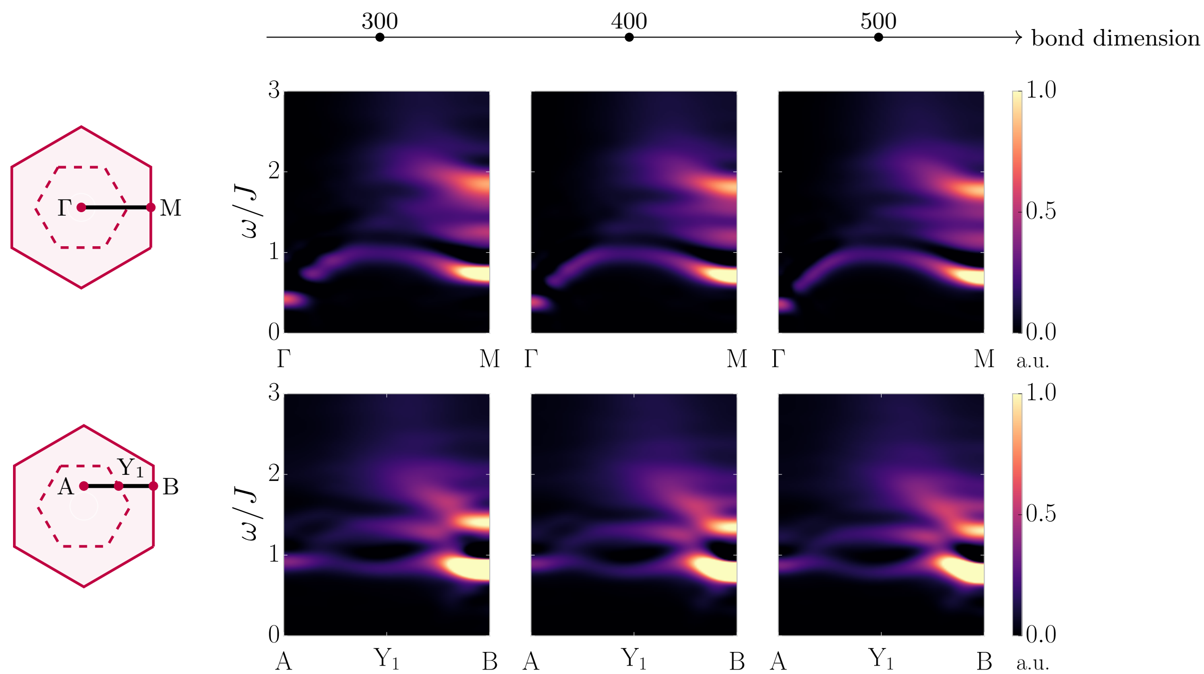

FIG. S2. Comparing the out-of-plane spectral functions for the TLHAF with anisotropy parameter $\delta = 0.05$ for three different bond dimensions.

determine the latter, we need $\chi > 500$, as we saw in Fig. S1 and Fig. S2. Fortunately, this is possible by time-evolving for a shorter period of time, which effectively broadens the spectral function. Such broadening usually makes it harder to pinpoint the location of the magnon dispersion, as the broadened lineshape merges with other features. However, at the lowest energies, the band is well-separated from such other features, and one can reliably extract its center from short-time data. This way we obtain values for ε_K up to $\chi = 800$, as shown in Fig. S3; these points allow one to roughly extrapolate $\varepsilon_K \approx 0.3J$ as $\chi \to \infty$.

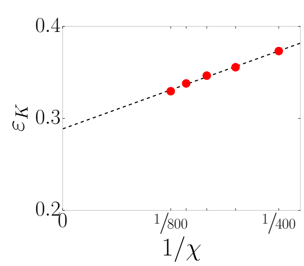

FIG. S3. Determining the energy of the near-Goldstone mode at the zone corner for anisotropy parameter $\delta = 0.05$. Extrapolating $\chi \to \infty$, we find $\varepsilon_K \approx 0.3J$.

B. Convergence in cylinder circumference

Given that the ground state order is 120°, circumferences which are not multiples of three would usually frustrate the ground state order—making it useless for the purpose of checking convergence. However, one can work in a local/rotating frame. More precisely, considering the Hamiltonian on the infinite lattice, one can rotate the spin by 120° degrees on the three sublattices; in these new variables, the $SU(2)$ symmetry of the Hamiltonian is no longer explicit, and one of the ground states looks like a ferromagnetic state. The beauty of this approach is that the Hamiltonian turns out to still be translation-invariant in these new variables, and hence one can sensibly put it on cylinders with circumferences that are *not* a multiple of three *without* frustrating the ground state order.

Hence, this allows us to compare the spectral functions for circumferences $L_{\rm circ} = 4, 5, 6$, giving a sense of convergence in this parameter. Note that the momentum slices we can access depend on the circumference (since it determines the quantization conditions on the momentum along the circumference); we can always access the momentum slice $\Gamma - M$, and for $L_{\rm circ}$ even, we can access the $C - M - C'$ slice, as shown in Fig. S4, which shows the results for the anisotropy $\delta = 0.1$.

Remarkably, in Fig. S4, we observe that the *single*-magnon dispersion is close to being converged in circumference, aside from the variations at the lowest energies. The multi-magnon continuum does show variations. For our purposes, it is important to emphasize that we do not use the properties of this continuum in our argument: we consistently determine the continuum from taking combinations of the (converged) single-magnon dispersion (as discussed in the main text and in section III A). Given that the single-magnon dispersion shows convergence in both bond dimension and system size, this is a reasonable way of figuring out where the continuum will be in the two-dimensional limit.

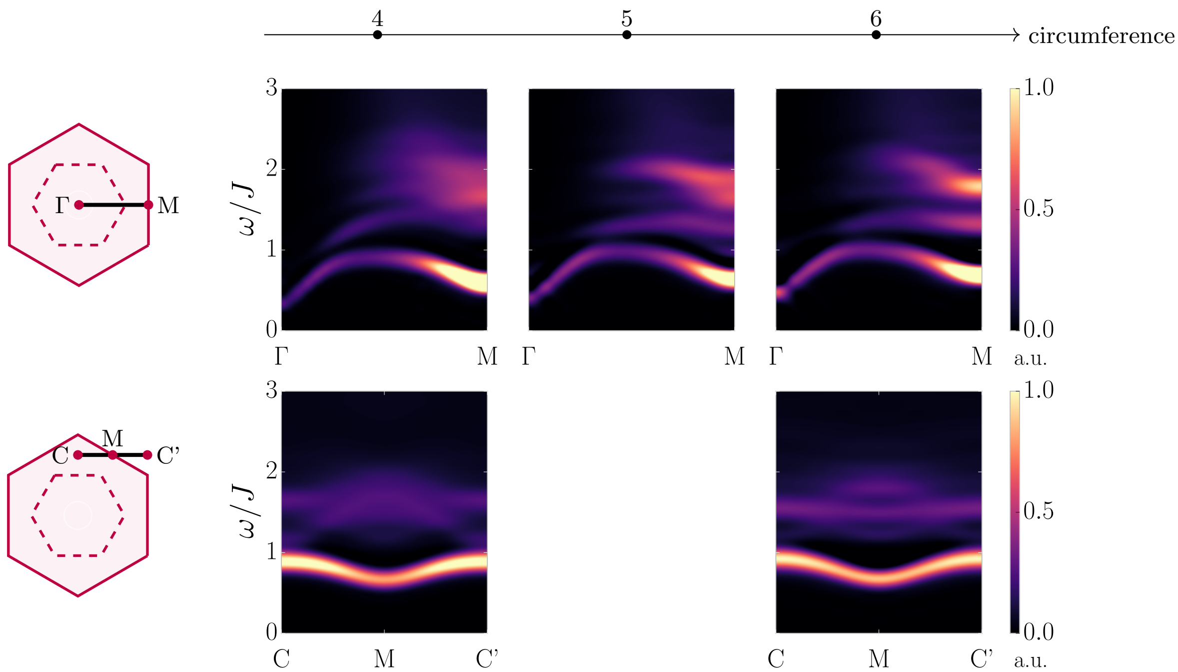

FIG. S4. Comparing the out-of-plane spectral functions for the TLHAF with anisotropy parameter $\delta = 0.1$ for three different cylinder circumferences.

Fig. S5 shows the analogous result for $\delta = 0.05$, which is the value of anisotropy discussed in the main text. We see that the single-magnon dispersion looks similar in all pictures, but at the same time, some variation is still noticeable. However, the bottom row (along the $C - M - C$) slice is more stable, hence this panel should give us a good estimate for the two-dimensional limit. We can use this as an independent measure of determining that the $L_{\rm circ} = 6$ is close to the two-dimensional limit: M appears in both the top and bottom rows, and whereas for $L_{\rm circ} = 4$ these two values disagree (indeed, despite both M points being symmetry-equivalent in the two-dimensional limit, they are *not* equivalent on the cylindrical geometry, which does not obey the six-fold rotation symmetry of the triangular lattice), for $L_{\rm circ} = 6$, these two values closely agree.

Another way of probing that the $L_{\rm circ} = 6$ is close to the two-dimensional limit as far as the single-magnon dispersion is concerned, is by comparing integrated weights. For example, for the top slice shown in Fig. S5, one can compare the weight in the multi-magnon sector at M compared to the weight in the single-magnon sector at that same point. For the circumferences $L_{\rm circ} = 4, 5, 6$, we find, respectively, the ratios 1.3, 2.6, and 2.6. This indicates that for the larger circumferences that we can probe, the multi-magnon sector is decoupled from the single-magnon band. This is reassuring, since as we have observed already, there are clear variations within the continuum.

Finally, fixing $L_{\rm circ} = 6$, there is an independent check we can perform regarding finite-circumference effects. As mentioned above, there are various points in the two-dimensional Brillouin zone which are symmetry-equivalent in the two-dimensional geometry, but which are no longer symmetry-equivalent on the cylindrical geometry. Fig. S6 shows such points: there are four pair of points (each denoted by a symbol) where the single-magnon energies must agree in the two-dimensional limit by symmetry arguments. Comparing the numerically obtained dispersions, we find that they differ by 3.1% (black diamonds), 4.8% (green squares), 5.7% (red dots) and 7.7% (blue triangles).

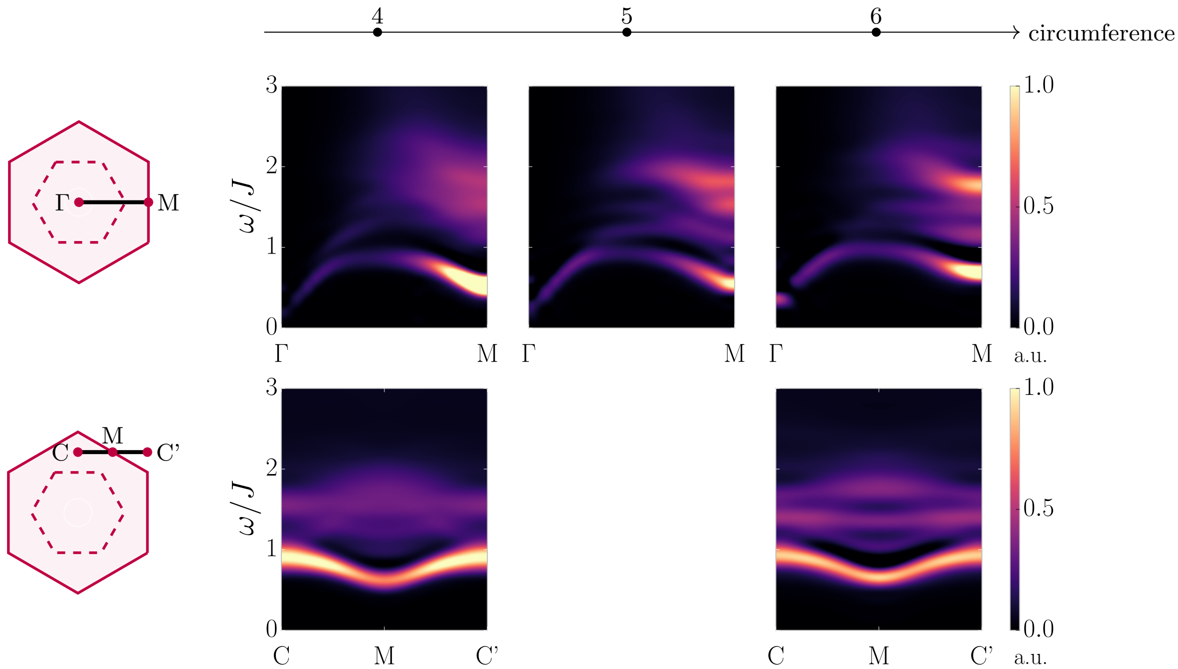

FIG. S5. Comparing the out-of-plane spectral functions for the TLHAF with anisotropy parameter $\delta = 0.05$ for three different cylinder circumferences.

Given that there would be no reason that these points would have similar energies aside from convergence toward the two-dimensional limit, we see these numbers as a reliable indication that we are close to said limit.

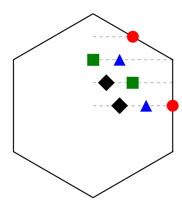

FIG. S6. Four pairs of points (accessible for $L_{\mathrm{circ}} = 6$) which are symmetry-equivalent in the two-dimensional limit, but which are not equivalent on the cylinder. Comparing the dispersion at these points gives an independent probe of finite-circumference effects.

IV. INTERPOLATING QUASIPARTICLE SPECTRUM TO 2D BRILLOUIN ZONE AND COMPARING TO THE EXPERIMENTAL DATA

Fig. S7(a) shows the data that we can numerically obtain for the magnon dispersion for a cylinder with circumference $L_{\mathrm{circ}} = 6$, where we have rotated and superimposed the data along three different directions. This is for $\delta = 0.05$. The fact that the values roughly agree when they spatially overlap indicates that the finite-circumference effects are not too strong (see also Fig. S6). We interpolated this data to the two-dimensional BZ to generate Fig. 3(c) in the main text.

To test our interpolation method, we can take the LSWT prediction (Fig. S7(b)) as a test case: restricting this to the same grid as is shown in Fig. S7(a) and then using our 2D interpolation method, we produce Fig. S7(c). We see that this closely agrees with the original dispersion in Fig. S7(b).

As indicated in the main text, the momentum slices we can access on our cylinder geometry are different from the direction in the experimental plot in Fig. 4(a) of the main text. However, since we have now interpolated our dispersion to the full two-dimensional BZ, we can take the same path as in the experimental plot. This is shown

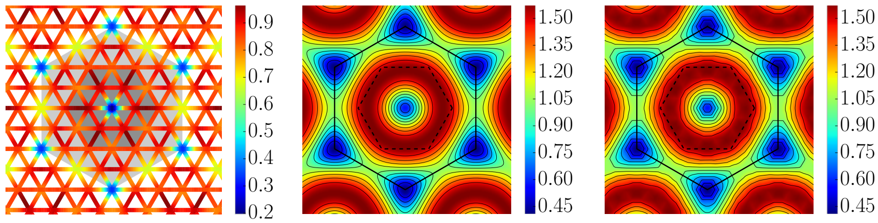

(a) (b) (c)

FIG. S7. (a) The dispersion for $\delta = 0.05$ that we obtained numerically (in units of J) before interpolating to 2D. (b) The LSWT prediction for $\delta = 0.05$ (in units of J). (c) The result of first restricting the aforementioned LSWT prediction onto the grid shown in (b) and then using our 2D interpolation method; the fact that this closely agrees with (c) is an indication that our interpolation method is reliable.

in Fig. 4(b) of the main text, where we also have included a second path that is related by translating by a vector K—this resembles what one would pick up if one measures the full dynamic structure factor, as opposed to just the out-of-plane component. In principle, Fig. 4(b) would have a third band which is the mirror image of the red curve ε_2, but this has been left out as to not clutter the image.